Acta Neuropathologica Communications

RESEARCH

Open Access

Mild traumatic brain injury induces microvascular injury and accelerates Alzheimer-like pathogenesis in mice

Yingxi Wu[1,2†], Haijian Wu[1,2,3†], Jianxiong Zeng[1,2], Brock Pluimer[1,2,4], Shirley Dong[1,2], Xiaochun Xie[1,2], Xinying Guo[1,2], Tenghuan Ge[1,2], Xinyan Liang[1,2,4], Sudi Feng[1,2], Youzhen Yan[1,2], Jian-Fu Chen[5], Naomi Sta Maria[1,2], Qingyi Ma[6], Fernando Gomez-Pinilla[7] and Zhen Zhao[1,2,4*]

Abstract

Introduction: Traumatic brain injury (TBI) is considered as the most robust environmental risk factor for Alzheimer's disease (AD). Besides direct neuronal injury and neuroinflammation, vascular impairment is also a hallmark event of the pathological cascade after TBI. However, the vascular connection between TBI and subsequent AD pathogenesis remains underexplored.

Methods: In a closed-head mild TBI (mTBI) model in mice with controlled cortical impact, we examined the time courses of microvascular injury, blood–brain barrier (BBB) dysfunction, gliosis and motor function impairment in wild type C57BL/6 mice. We also evaluated the BBB integrity, amyloid pathology as well as cognitive functions after mTBI in the 5xFAD mouse model of AD.

Results: mTBI induced microvascular injury with BBB breakdown, pericyte loss, basement membrane alteration and cerebral blood flow reduction in mice, in which BBB breakdown preceded gliosis. More importantly, mTBI accelerated BBB leakage, amyloid pathology and cognitive impairment in the 5xFAD mice.

Discussion: Our data demonstrated that microvascular injury plays a key role in the pathogenesis of AD after mTBI. Therefore, restoring vascular functions might be beneficial for patients with mTBI, and potentially reduce the risk of developing AD.

Keywords: Traumatic brain injury, Alzheimer's disease, Microvascular injury, Blood–brain barrier, β-amyloid

Background

Alzheimer's disease (AD) is an age-related progressive neurodegenerative condition, manifesting amyloid plaque and neurofibrillary tangle formation, neurovascular and neuroimmune dysfunctions, and cognitive impairment [1]. While advanced aging increases the likelihood of AD, genetic inheritance and environmental risk factors also contribute significantly [2]. For example, Traumatic brain injury (TBI) is considered as the most robust environmental risk factor for AD [3]. TBI is a leading cause of death and disability, particularly in young adults, resulting in a great impact on productivity and dependence on health care in later life [4]. Both clinical and preclinical studies have demonstrated that TBI triggers multiple neurodegenerative cascades, including axonal and dendritic damage, excitatory toxicity, neuroinflammation and cell death [5], as well as cerebrovascular impairment such as edema, circulatory insufficiency, and blood–brain barrier (BBB)

*Correspondence: zzhao@usc.edu
†Yingxi Wu and Haijian Wu contributed equally
[1] Center for Neurodegeneration and Regeneration, Zilkha Neurogenetic Institute, Room: 241, 1501 San Pablo Street, Los Angeles, CA 90033, USA
Full list of author information is available at the end of the article

breakdown [6], exhibiting a high similarity with AD [4]. TBI is highly prevalent during military service and contact sports, and doubles the risk of developing AD and dementia [7]. More importantly, it also exacerbates certain pathological events that are specific to AD, including the brain's overproduction and accumulation of β-amyloid (Aβ), and neurofibrillary tangles consisting of hyperphosphorylated Tau [8, 9]. Yet the underlying mechanisms remain elusive.

Histological and neuroimaging assessments have demonstrated that microvascular injury with BBB breakdown are common in TBI patients. It occurs during the acute/subacute phase of TBI [10, 11] and may last for years in nearly 50% of the survivors [12, 13], resulting in long-term brain dysfunctions. Such microvascular endophenotype was well recapitulated in animal models of TBI [4], including fluid percussion injury, controlled cortical impact and blast injury. Mechanistically, TBI induces endothelial dysfunction [14], disrupts the crosstalk between endothelial cells and pericytes [15], reduces cerebral blood flow (CBF) and causes tissue hypoxia [16], upregulation of vascular endothelial growth factor (VEGF) and metallopeptidases [17, 18], leukocyte infiltration [19], gliosis and neuroinflammation [5], which all contribute to BBB dysfunctions.

As the interface between the circulation and central nervous system (CNS), the BBB plays a key role in normal brain physiological regulation and homeostasis [20]. Microvascular injury often results in a cascade of events including extravasation of plasma proteins that are potentially toxic to neuronal cells, parenchymal edema and hypoxia, metabolic stress including endoplasmic reticulum (ER) and mitochondrial stress, accumulation of metabolic wastes, activation of microglia and astrocytes, and eventually neuronal dysfunctions [20, 21]. Although microvascular injury is a shared endophenotype between TBI and AD [4], and a strong modifier of AD pathogenesis and progression [21], the vascular link between TBI and AD has not been investigated in depth.

Since mild TBI (mTBI) represents nearly 85% of cases, we applied a close-head mTBI model in rodents to investigate vascular impairment after mTBI, as well as to understand its link to AD pathogenesis. We found that mTBI induced microvascular injury and BBB dysfunction in the acute/subacute phase after injury, which was tightly associated with circulatory insufficiency and pericyte loss, and in general preceded astrogliosis and microglia activation. In addition, applying mTBI in 5xFAD transgenic model of AD demonstrated that mTBI accelerated BBB disruption, amyloid pathology and cognitive impairments. Therefore, improving vascular functions and BBB integrity in patients with mTBI may be beneficial and even reduce the risk of developing AD.

Methods

Animals

12–16 weeks old C57BL/6 mice and 5xFAD mice were used (Additional File 1: Fig. 1A). 5xFAD mouse model is a well-characterized mouse model of AD, with expression of human *APP* and *PSEN1* transgenes with a total of five AD-linked mutations: the Swedish (K670N/M671L), Florida (I716V), and London (V717I) mutations in APP, and the M146L and L286V mutations in PSEN1 [22]. All procedures are approved by the Institutional Animal Care and Use Committee at the University of Southern California using the US National Institutes of Health (NIH) guidelines.

Randomization and blinding

All animals were randomized for their genotype information and surgical procedures, and included in the analysis. The operators responsible for the experimental procedures and data analysis were blinded and unaware of group allocation throughout the experiments.

Closed-head mTBI mouse model

Mice received a mild closed-head impact following the procedures previously reported with minor modifications [23]. Briefly, for a precise impact mimicking mTBI, we utilized a stereotactic frame with adjustable angle (Stereotaxic Alignment System, KOPF) to ensure the impacted surface (the impact central point at Bregma − 2 mm and lateral 2.5 mm) of the skull was presented perpendicular to the impactor (Additional File 1: Fig. 1b, Brain and Spinal Cord Impactor, #68099, RWD Life Science). We also custom-made plastic flat-tip impactor (RWD Life Science) to reduce the impact. Mice were anesthetized with ketamine/xylazine (90 mg/kg, 9 mg/kg; i.p.), then the head was fixed with a 15° angle, and a gel pad was placed under the head in order to maximally avoid the skull fractures and intracerebral bleeding. An incision was made to expose skull surface after anesthesia and then the mice were subjected to an impact using a 4 mm plastic flat-tip impactor. The velocity was 3 m/s, the depth was 1.0 mm and the impact duration was 180 ms (see Additional File 1: Fig. 1c–d). After the procedure, the mice were put back to their cages with heating to recover from the anesthesia. For sham-operated mice, the same procedure was performed as the mTBI group except the tip was set 2.0 mm above the skull.

Open-head severe TBI (sTBI) mouse model

Mice received the sTBI following the procedures previously reported [24]. Briefly, mice were anesthetized with ketamine/xylazine (90 mg/kg, 9 mg/kg; i.p.), and the mouse head was then fixed in the stereotactic frame (Stereotaxic Alignment System, KOPF). A craniotomy

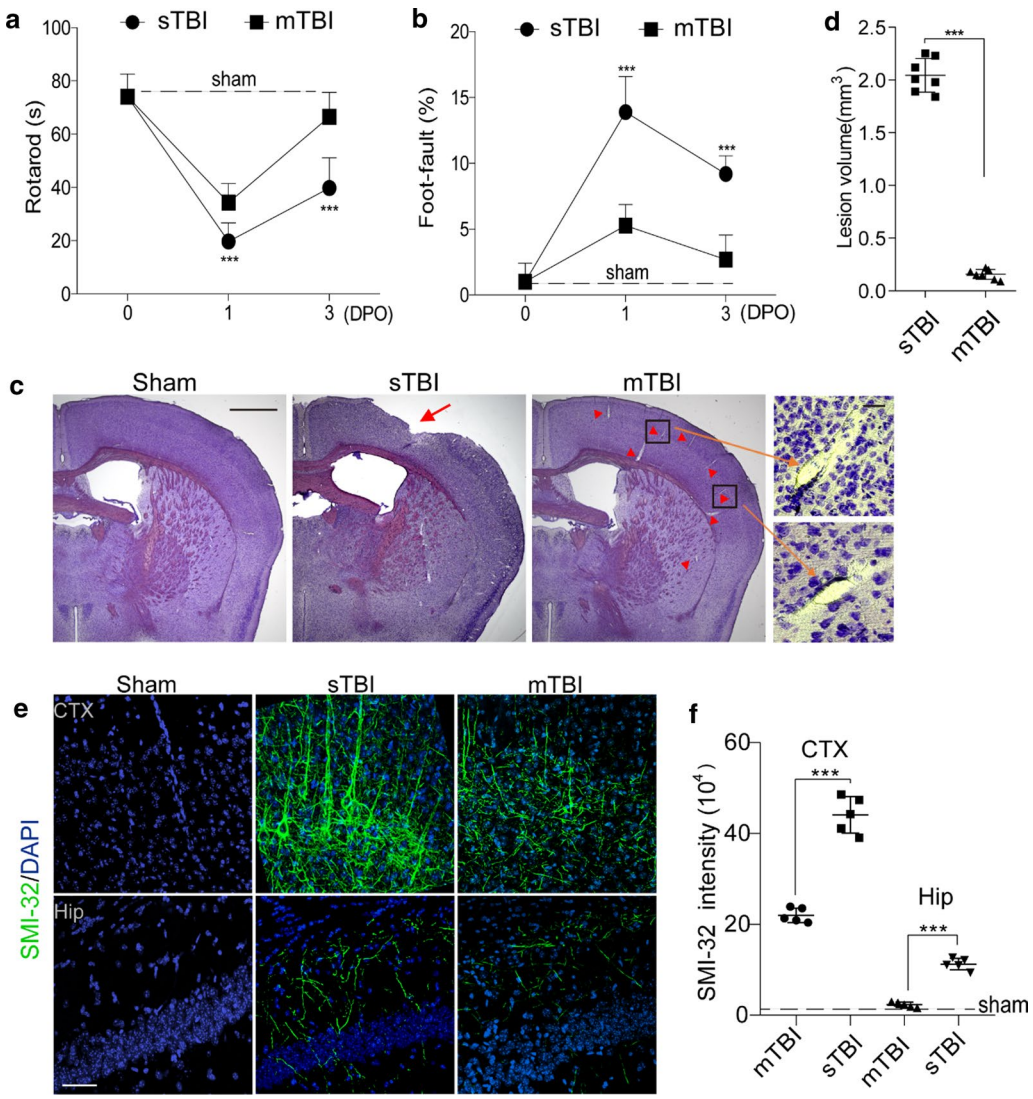

Fig. 1 Traumatic brain injury models with controlled cortical impact in mice. **a**–**b** Rotarod test (**a**) and foot-fault test (**b**) were performed on 0, 1 day and 3 days post operation (DPO) in sTBI mice ($n = 8$) or mTBI mice ($n = 7$). Dash lines indicate average value from sham-operated group ($n = 5$). In **a**–**b** mean ± SD; ***, $P < 0.001$ between sTBI and mTBI groups; NS, non-significant ($P > 0.05$), one-way ANOVA followed by Bonferroni's post-hoc tests. **c** Representative images of cresyl violet staining of brain sections from sham-operated, sTBI and mTBI mice. Scale bar = 1 mm (left), and 50 μm (right) in high magnification. Arrow indicates cortical lesion; arrowhead indicates enlarged perivascular space. **d** Quantification of TBI-induced lesion volume at 24 h post-injury in sTBI mice and mTBI mice. The injury resulted in a significantly larger lesion volume in sTBI mice when compared with mTBI mice. $n = 7$ mice per group. **e**–**f** Representative images **e** of fluorescence immunostaining for SMI-32 (green) and DAPI (blue), quantification of SIM-32 fluorescence intensity **f** in cortex (CTX) and hippocampus (Hip) of sham-operated, sTBI and mTBI mice 3 days after injury. Scale bar = 50 μm, $n = 5$ mice in sham-operated, sTBI and mTBI group respectively. In **d**, **f**, Mean ± SD; ***, $P < 0.001$ by Student's *t*-test

was made using a drill and 4.5-mm trephine in the center between Lambda and Bregma, and then the bone flap was removed. Mice were subjected to an impact using a 4 mm metal flat-tip impactor (Brain and Spinal Cord Impactor, #68099, RWD Life Science). The impact central point was Bregma − 2.5 mm and lateral 2.5 mm. The velocity was 3 m/s, the depth was 1 mm and the impact duration was 180 ms. Then the scalp was closed with suture, and the mice were put back to their cages to recover from the anesthesia. For sham-operated mice, the same procedure was performed as the sTBI group except the tip was set 2.0 mm above the skull.

Behavioral tests

Rotarod test

Mice were trained on an accelerating (5–20 rpm) rotating rod (rotarod) for 3 days before TBI. Test sessions consist of six trials at a variable speed (an initial velocity of 5 rpm was used for the first 10 s, a linear increase from 5 to 10 rpm for the next 30 s, and a linear increase from 10 to 20 rpm between 40 and 80 s). The final score was determined as the mean time that a mouse was able to remain on the rod over six trials.

Foot fault test

The foot-fault test was performed as previously described [25]. Mice were placed on hexagonal grids of different sizes. Mice placed their paws on the wire while moving along the grid. With each weight-bearing step, the paw may fall or slip between the wire. This was recorded as a foot fault. The total number of steps (movement of each forelimb) that the mouse used to cross the grid was counted, and the total number of foot faults for each forelimb was recorded.

Contextual fear conditioning

A hippocampus-dependent fear conditioning test was performed as previously described [26]. The experiments were performed using standard conditioning chambers housed in a soundproof isolation cubicle and equipped with a stainless-steel grid floor connected to a solid-state shock scrambler. The scrambler was connected to an electronic constant-current shock source that was controlled via Freezeframe software (Coulbourne Instruments). A digital camera was mounted on the steel ceiling and behavior was monitored. During training, mice were placed in the conditioning chamber for 4 min and received two-foot shocks (0.25 mA, 2 s) at 1-min interval starting 2 min after placing the mouse in the chamber. Contextual memory was tested the next day in the chamber without foot shocks. Hippocampus-dependent fear memory formation was evaluated by scoring freezing behavior (the absence of all movement except for respiration). For the contextual fear conditioning paradigms, the automated Freezeframe system was used to score the percentage of total freezing time with a threshold set at 10% and minimal bout duration of 0.25 s.

Determination of lesion volume

Mouse brains were cut into serial 20 μm cryostat sections. Every 10th section was stained with cresyl violet and the lesion area was determined using the Image J analysis software. Sections were digitized and converted to gray scale, and the border between TBI and non-TBI tissue was outlined. The lesion volume was calculated by subtracting the volume of the non-lesioned area in the ipsilateral hemisphere from the volume of the whole area in the contralateral hemisphere and expressed in mm^3 as previously described [27].

Assessment of edema

Brain water content is a sensitive measure of cerebral edema which was determined using the wet/dry method as previously described [27]. Mice were decapitated and brains were rapidly removed from the skull. The fresh brain was weighed in 3 mm coronal sections of the ipsilateral cortex, centered upon the impact site, then dehydrated for 24 h at 110 °C and reweighed. The percentage of brain water content was calculated using the following formula: (wet weight − dry weight)/(wet weight) × 100.

Tracer injection to detect BBB leakage

Mice were injected via the tail vein with Alexa Fluor 555-cadaverine (6 μg/g; Invitrogen, A30677) [28] dissolved in saline 1, 3 and 8 days after mTBI. After 2 h mice were anesthetized and perfused with phosphate-buffered saline (PBS) at pH 7.4, and the brains were collected.

Evaluation of BBB permeability

BBB permeability was assessed by measuring the extravasation of Evans Blue dye as described previously [29]. 24 h after TBI injury, the mice were anesthetized, and Evans Blue dye (2% in saline) was injected slowly through the jugular vein (4 mL/kg) and allowed to circulate for 1.5 h before sacrifice.

Laser speckle contrast imaging (LSCI)

LSCI is based on the blurring of interference patterns of scattered laser light by the flow of blood cells to visualize blood perfusion in the microcirculation instantaneously [30]. Briefly, mice were anesthetized with gas anesthesia (isoflurane 2% in oxygen), with the head fixed in a stereotaxic frame (Kopf Instruments) and placed under an RFLSI Pro (RWD life sciences) and maintained at 1.2% isoflurane throughout the experiment. The surface of the skull is illuminated with a 784-nm 32-mW laser (RWD life science) at a 30° angle with a beam expander and light intensity controlled by a polarizer. Blood flow is detected by a CCD camera and the image acquisition is performed using custom software (RWD life science). Three hundred frames are acquired at 10 Hz with 10-ms exposure time. For the assessment of speckle contrast over time, regions of interest (ROIs) were selected and centered at the site where the laser is targeted on the cortex.

Immunohistochemistry and confocal microscopy analysis

At endpoint, mice were anesthetized and transcardially perfused with PBS, and mouse brains were extracted and fixed for 12 h in 4% paraformaldehyde (PFA) in PBS at

4 °C. 20 μm-thick coronal cryosections were used for immunohistochemistry in this study. After washing with PBS, brain sections were permeabilized and incubated in 5% Donkey Serum for 1 h for blocking. Then the brain tissues were incubated in primary antibody overnight at 4 °C. The primary antibody information is as following: anti-Fibrinogen antibody (1:200, Dako, A0080), anti-Iba1 antibody (1:500, Wako, 019-19741), anti-NeuN antibody (1:200, Abcam, ab177487), anti-Glial fibrillary acidic protein (GFAP) antibody (1:200, Invitrogen, 13-0300), anti-SMI-32 antibody (1:1000, Biolegend, 801709), anti-Cluster of differentiation (CD13) antibody (1:200, R&D Systems, AF2335), anti-β amyloid antibody (1:200, #D54D2, Cell Signaling). After washing off the primary antibody with PBS, the brain sections were then incubated with secondary antibodies (1:500; Jackson Immunoresearch Laboratories) for 1 h at room temperature. Dylight 488 conjugated-lectin (1:200, Vector, DL1174) was used to label brain vasculature, and Alexa Fluor 647 Donkey anti-Mouse IgG (1:500; Invitrogen, A-31571) was used to detect extravasation of IgG. After that, the sections were rinsed with PBS and covered with fluorescence mounting medium with DAPI (4′,6-diamidino-2-phenylindole; Vector Laboratories, #H-1200).

Detection of apoptosis

TUNEL assay was performed according to the manufacturer's protocol (CAS7791-13-1, Roche). Tissues were incubated with the TUNEL reaction mixture in a humidified chamber for 30 min at 37 °C in the dark.

Detection of Aβ plaques

After PFA fixation, the sections were incubated in 1% aqueous Thioflavin S (T1892; Sigma) for 5 min and rinsed in 80% ethanol, 95% ethanol, and distilled water. All images were taken with the Nikon A1R confocal microscopy and analyzed using NIH ImageJ software. In each animal, 4 randomly selected fields in the cortex and hippocampus in TBI-affected hemisphere were analyzed in 4 non-adjacent sections (~ 100 μm apart) and averaged per mouse.

Cresyl violet staining

The brain tissue sections were firstly fixed by methanol for 5 min, then stained with the Cresyl Echt Violet staining kit (American MasterTech, catalog # AHC0443) and incubated for 5 min; next, the slides were rinsed in 2 changes of distilled water (15 s each) to remove the excess stain; then the slides were rinsed using 100% ethanol (10 s). At last, the slides were coverslipped with mounting medium.

Extravascular IgG, fibrinogen and fibrin deposits

We used antibodies that detected IgG, fibrinogen and fibrinogen-derived fibrin polymers (see Immunohistochemistry). Ten-micron maximum projection z-stacks were reconstructed, and the IgG, fibrinogen and fibrin-positive perivascular signals on the abluminal side of lectin-positive endothelial profiles on microvessels ≤ 6 μm in diameter were analyzed using ImageJ. In each animal, 4–5 randomly selected fields in the cortex in both mTBI-affected hemisphere and unaffected contralateral hemisphere were analyzed in 4 non-adjacent sections (~ 100 μm apart) and averaged per mouse.

Analysis for SMI-32

Ten-micron maximum projection z-stacks were reconstructed, and the SMI-32 signals were analyzed using ImageJ. In each animal, 4 randomly selected fields in the cortex and hippocampus in TBI-affected hemisphere were analyzed in 4 non-adjacent sections (~ 100 μm apart) and averaged per mouse.

GFAP-positive astrocytes and Iba1-positive microglia counting

For quantification, GFAP-positive astrocytes or Iba1-positive microglia that also co-localized with DAPI-positive nuclei were quantified by using the Image J Cell Counter analysis tool. In each animal 5 randomly selected fields from the cortex were analyzed in 4 non-adjacent sections (~ 100 μm apart). The number of GFAP-positive astrocytes was expressed per mm^2 of brain tissue. The activated microglia undergo morphological changes including retraction of the processes and acquisition of a phagocytotic shape, but the quiescent microglia exhibit a ramified morphology [31].

NeuN-positive neuronal nuclei counting

For quantification, NeuN-positive neurons were quantified by using the Image J Cell Counter analysis tool. In each animal, 5 randomly selected fields from the cortex were analyzed in 4 nonadjacent sections (~ 100 μm apart). The number of NeuN-positive neurons colocalized with TUNEL was counted followed by the same procedure.

Quantification of pericyte numbers and coverage

The quantification analysis of pericyte numbers and coverage was restricted to CD13-positive perivascular mural cells that were associated with brain capillaries defined as vessels with ≤ 6 μm in diameter. For pericyte numbers, ten-micron maximum projection z-stacks were reconstructed, and the number of CD13-positive perivascular cell bodies that co-localized with

DAPI-positive nuclei on the abluminal side of lectin-positive endothelium on vessels ≤ 6 μm counted using ImageJ Cell Counter plug-in. In each animal, 4–5 randomly selected fields in the cortex regions were analyzed in 4 non-adjacent sections (~ 100 μm apart) and averaged per mouse. The number of pericytes was expressed per mm^2 of tissue. For pericyte coverage, ten-micron maximum projection z-stacks were reconstructed, and the areas occupied by CD13-positive (pericyte) and lectin-positive (endothelium) fluorescent signals on vessels ≤ 6 μm were subjected separately to threshold processing and analyzed using ImageJ as previously described [32]. In each animal, 4–5 randomly selected fields in the cortex regions were analyzed in 4 nonadjacent sections (~ 100 μm apart) and averaged per mouse.

Microvascular capillary length

Ten-micron maximum projection z-stacks were reconstructed, and the length of lectin-positive capillary profiles (≤ 6 μm in diameter) was measured using the ImageJ plugin "Neuro J" length analysis tool. In each animal, 4–5 randomly selected fields in the cortex were analyzed from 4 nonadjacent sections (~ 100 μm apart) and averaged per mouse. The length was expressed in mm of lectin-positive vascular profiles per mm^3 of brain tissue.

Aβ deposits calculation Aβ-positive areas were determined using ImageJ software. Briefly, the images were taken on a BZ9000 fluorescent microscope in single plain at 20× and subjected to threshold processing (Otsu) using ImageJ, and the percent area occupied by the signal in the image area was measured as described previously [26]. In each animal, four randomly selected fields from the cortex and hippocampus were imaged and analyzed in four non-adjacent sections (~ 100 μm apart).

Western blot

The total proteins from cortical tissue of TBI-affected hemisphere in sham-operated, sTBI and mTBI mice were extracted, and Synapsin I was analyzed by Western blot. Briefly, protein samples were separated by electrophoresis on a 10% polyacrylamide gel and electrotransferred to a nitrocellulose membrane. Nonspecific binding sites were blocked in TBS, overnight at 4 °C, with 2% BSA and 0.1% Tween-20. Membranes were rinsed for 10 min in a buffer (0.1% Tween-20 in TBS) and then incubated with anti-synapsin I (1:1500, Sigma) followed by anti-rabbit IgG horseradish peroxidase conjugate (Santa Cruz Biotechnology). After rinsing with buffer, the immunocomplexes were developed with G:BOX Chemi XX6 gel doc system (Syngene) and analyzed in Image Lab software. β-Actin was used as an internal control for Western blot.

Statistical analysis

Sample sizes were calculated using nQUERY assuming a two-sided alpha-level of 0.05, 80% power, and homogeneous variances for the 2 samples to be compared, with the means and common standard deviation for different parameters predicted from published data and pilot studies. For comparison between two groups, the F test was conducted to determine the similarity in the variances between the groups that are statistically compared, and statistical significance was analyzed by Student's *t*-test. For multiple comparisons, Bartlett's test for equal variances was used to determine the variances between the multiple groups and one-way analysis of variance (ANOVA) followed by Bonferroni's post hoc test was used to test statistical significance. All analyses were performed using GraphPad Prism 8 software by an investigator blinded to the experimental conditions. A p-value < 0.05 was considered as statistically significant.

Results

Microvascular injury in a mouse model of mTBI

To determine the vascular impairment in mTBI, we first compared the pathological changes and functional performances in an open-head severe TBI (sTBI) model with a close-head mTBI model, based on controlled cortical impact (Additional File 1: Fig. 1). Consistent with previous studies [33], the sTBI model induced strong deficits in motor function, as seen on both rotarod test and foot-fault test (Fig. 1a, b); whereas the mTBI model only induced transient motor impairments, as the mice nearly recovered in 3 days in the same behavioral tests (Fig. 1a, b). In line with the behavioral outcomes, mTBI model didn't cause prominent cortical lesion at 24 h post-injury, when compared to the sTBI model with an average lesion volume of over 2 mm^3 (Fig. 1c, d). Brain water content, as a measure of cerebral edema, was not significantly changed 24 h after mTBI either (Additional File 1: Fig. 2a). In addition, we observed very few TUNEL- and NeuN- double-positive cells in the mTBI impacted ipsilateral cortex at 3 days after mTBI (Additional File 1: Fig. 2b–c); while ~ 20% neuronal death was found near the cortical lesion in the sTBI model (Additional File 1: Fig. 2b–c).

Interestingly, axonal injury was detectable 3 days after mTBI in both mTBI-affected ipsilateral cortex and hippocampus (Fig. 1e), based on a monoclonal SMI-32 antibody against non-phosphorylated neurofilament [34], although to a much lesser extent than that found in sTBI (Fig. 1e, f). Western blotting of synaptic marker synapsin I also showed a ~ 32% reduction in mTBI-affected ipsilateral cortex, compared to a 75% reduction after sTBI (Additional File 1: Fig. 2d–e). Microglia and astrocytes were much less activated in both mTBI-affected

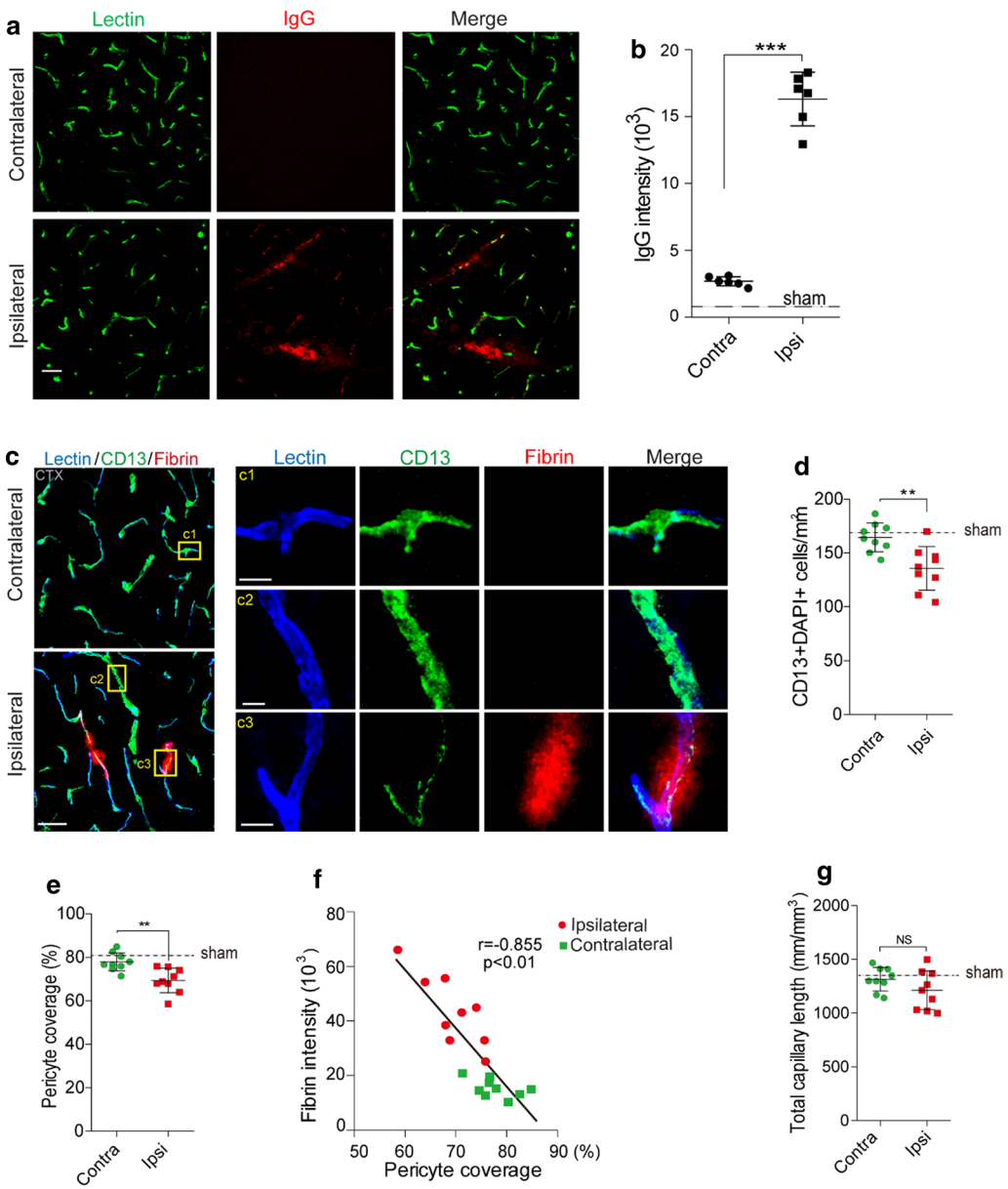

Fig. 2 Altered pericyte coverage in mTBI mice. **a**–**b** Representative images (**a**) and quantification (**b**) showing extravasation of plasma IgG (red) in brain parenchyma 3 days after mTBI. n = 6 mice. Dash line indicates an average value from sham-operated group ($n = 5$ mice). Scale bar = 50 μm. **c** Representative images showing CD13-positive pericyte coverage (green), lectin-positive endothelial vascular profiles (blue) and extravasation of fibrin deposits (red) in brain parenchyma of mTBI-affected ipsilateral side or contralateral side 3 days after mTBI. Scale bar = 50 μm. Insert on right: high magnification images of boxed regions in (c1–c3), Scale bar = 10 μm. **d**–**e** Quantification of CD13-positive pericyte cell bodies per mm^2 (**d**) and pericyte coverage on lectin microvessel profiles (**e**) in brain parenchyma of mTBI-affected ipsilateral side and contralateral side 3 days after mTBI. $n = 9$ mice per group. **f** Pearson's correlation plot between BBB impairment based on fibrin deposits and loss of pericyte coverage in brain parenchyma 3 days after mTBI. $n = 18$ hemispheres. r = Pearson's coefficient. *P*, significance. **g** Quantification of microvascular density in the cortexes of mTBI-affected ipsilateral side and contralateral side 3 days after mTBI. $n = 9$ mice per group. Mean ± SD in **b**, **d**–**e**, **g**; **, $P < 0.01$; ***, $P < 0.001$; NS, non-significant ($P > 0.05$) by Student's *t*-test

ipsilateral cortical areas and contralateral area, when compared with sTBI-affected ones (Additional File 1: Fig. 3). Unlike sTBI, the microglial activation and astrogliosis did not spread much to the contralateral hemisphere at 3 days after mTBI (Additional File 1: Fig. 3b, d).

BBB breakdown is a hallmark of TBI, which occurs acutely within hours after tissue damage and lasts for

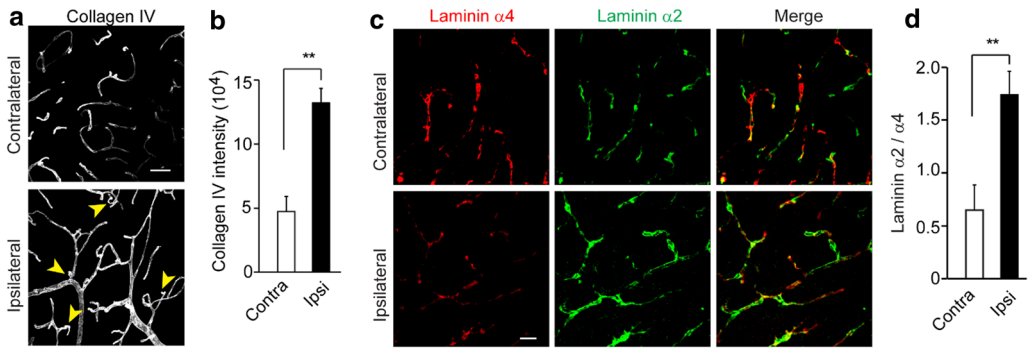

Fig. 3 Basement membrane structural change in mTBI mice. **a**–**b** Representative confocal microscope images (**a**) and quantification (**b**) showing upregulation of collagen IV in mTBI-impacted ipsilateral cortical area 3 days after mTBI compare to contralateral side. Scale bar = 50 µm. **c** Representative confocal microscope images showing differential laminin α2 and α4 levels in mTBI-impacted ipsilateral cortical area and contralateral side 3 days after mTBI. **d** Quantification of α2 and α4 ratio based on fluorescent intensities in mTBI-impacted ipsilateral cortical area compare to contralateral side. Scale bar = 30 µm. $n = 6$ mice per group. Mean ± SD in **b**, **d**; **, $P < 0.01$; ***, $P < 0.001$; NS, non-significant ($P > 0.05$) by Student's *t*-test

days [35]. As cresyl violet staining showed vascular segments with morphological impairment in brain sections from mTBI mice (Fig. 1c, arrowheads and inserts), we next performed histological analysis to examine the microvascular injury and BBB dysfunction occurred in the acute/subacute phase of mTBI. Immunostaining for plasma-derived IgG (Fig. 2a) demonstrated a ~six-fold increase in perivascular IgG deposits in the mTBI impacted cortical area 3 days after mTBI (Fig. 2b). We also found similar results in extravascular fibrin deposits (Additional File 1: Fig. 4a, b), or extravasation of exogenous tracer 555-cadaverine [28] (Additional File 1: Fig. 4c–d), suggesting BBB is compromised after mTBI, which is consistent with findings in human patients and different animal models [6].

mTBI resulted in pericytes loss and basement membrane alteration

Pericytes play a key role in regulating neurovascular functions of the brain including formation and maintenance of the BBB [28]. We found a substantial loss of brain pericytes based on the number of CD13-positive cells (Fig. 2c, d) in the impacted ipsilateral side 3 days after mTBI, when compared with unaffected contralateral hemisphere, as well as a reduction of pericyte coverage based on CD13 profile on Lectin-positive endothelial profiles (Fig. 2e). This pericyte loss is even more evident in microvascular segment with strong fibrin deposits (Fig. 2c inserts). More importantly, accumulation of perivascular fibrin deposits in mTBI mice correlated tightly with the reductions in pericyte coverage (Fig. 2f). However, there was no significant change in the total capillary length between impacted ipsilateral hemisphere and unaffected contralateral hemisphere (Fig. 2g), suggesting acute vascular rarefication perhaps is more specific to moderate and severe TBI [36]. Furthermore, the pathological changes of BBB in the acute/subacute phase of mTBI was associated with microcirculation insufficiency, as LSCI showed a ~50% reduction in CBF in the impacted cortex 3 days after mTBI (Additional File 1: Fig. 4e, f).

Recent genetic profiling studies in rodents indicated a TBI-induced genomic response in genes associated with the extracellular matrix proteins and basement membrane structures [37, 38]. We then performed histological analysis for different markers of perivascular compartments and extracellular basement membrane. Collagen IV, secreted by endothelial cells, mural cells and astrocytes, is a marker for both inner and outer basement membranes in the perivascular space [39]. It was significantly increased by 2.9-fold in mTBI-affected hemisphere compared to the unaffected contralateral side of the brain (Fig. 3a, b). More interestingly, we found immunostaining for vascular laminin α4 [40] was dramatically reduced in the mTBI-affected hemisphere when compared with the unaffected contralateral hemisphere (Fig. 3c), which is consistent with vascular injury and suggests vascular compartment within the perivascular space decreased after mTBI. In addition, laminin α2 immunoreactivity around the astrocytic endfeet of microvessels [41] was dramatically increased in mTBI-affected hemisphere compared to the unaffected contralateral hemisphere (Fig. 3c), indicating that the parenchymal compartment of the perivascular space increased after mTBI. Therefore, the ratio of

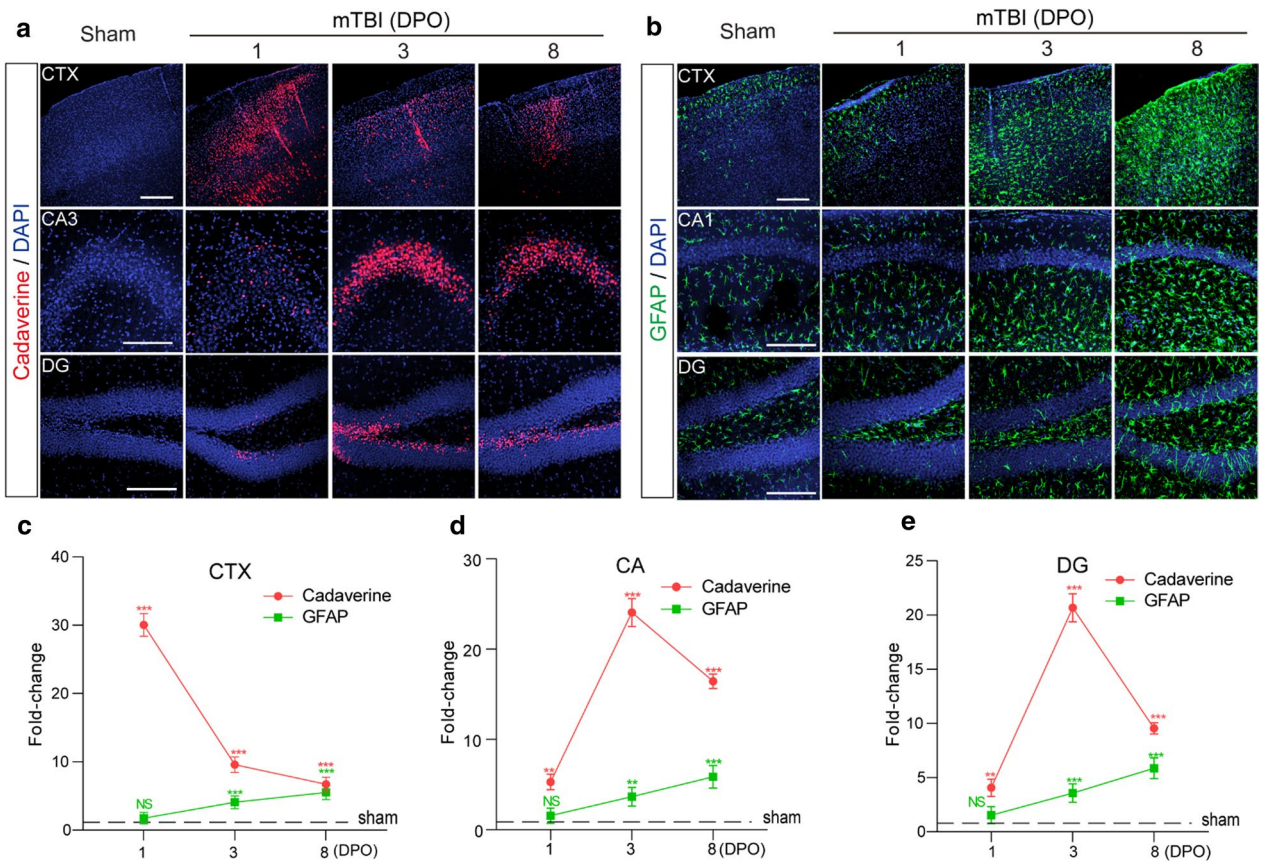

Fig. 4 The time courses of BBB dysfunction and astrogliosis after mTBI in mice. **a** Representative confocal microscope images showing the extravasation of intravenously administrated Alexa-555 cadaverine (red) in cortex (CTX), Cornu Ammonis 3 (CA3) and dentate gyrus (DG) area 1-day, 3- and 8- days post operation (DPO). Scale bar = 100 μm. **b** Representative confocal microscope images showing GFAP-positive astrocytes (green) in cortex (CTX), CA1 and dentate gyrus (DG) area 1-day, 3- and 8- days post operation (DPO). Scale bar = 100 μm. **c**–**e** Quantification for the fold changes for cadaverine intensity ($n = 5$ mice per time point) and GFAP positive cells ($n = 5$ mice per time point) in CTX area, CA area and DG area 1-day, 3- and 8- days post operation (DPO). In **c**–**e**, data are presented as mean ± SD; ***, $P < 0.001$; **, $P < 0.01$ NS, non-significant ($P > 0.05$) compare to sham group, one-way ANOVA followed by Bonferroni's post-hoc tests. Dash lines indicate the sham-operated group

laminins α2/α4 may potentially reflect the perivascular structural changes after mTBI (Fig. 3d).

mTBI induced BBB dysfunction precedes gliosis

To examine the time course of cerebrovascular impairment and BBB dysfunction in mTBI mice, we performed in vivo tracing of systemically administrated Alexa Fluor 555-cadaverine [28], on 1 day, 3- and 8-days post operation (DPO). We found that a severe BBB impairment in the impacted cortex area at 1 DPO (Fig. 4a), before astrogliosis and microglial activation became substantial (Fig. 4b, Additional File 1: Fig. 5a). More specifically, cadaverine tracer indicated a ~30.1-fold increase in parenchymal uptake in the ipsilateral cortex, which recovered gradually over 8 days (Fig. 4c). On the other hand, the BBB impairment in the hippocampal area appeared at 1 DPO, but peaked around 3 DPO as indicated by ~24.1-fold and ~20.7-fold increase of uptake in CA3 and dentate gyrus (DG) areas, respectively (Fig. 3d, e). On the other hand, immunostaining for GFAP-positive astrocytes (Fig. 4b) and Iba1-positive microglial cells (Additional File 1: Fig. 5a) indicated that astrocytes and microglial cells were significantly activated between 3 and 8 DPO after mTBI in both cortex and hippocampus (CA1 and DG) areas (Fig. 4c–e and Additional File 1: Fig. 5b–d), when compared with sham-operated group. Therefore, our data indicate that microvascular injury and BBB dysfunction preceded astrogliosis and microglial activation in the acute/subacute phase of mTBI.

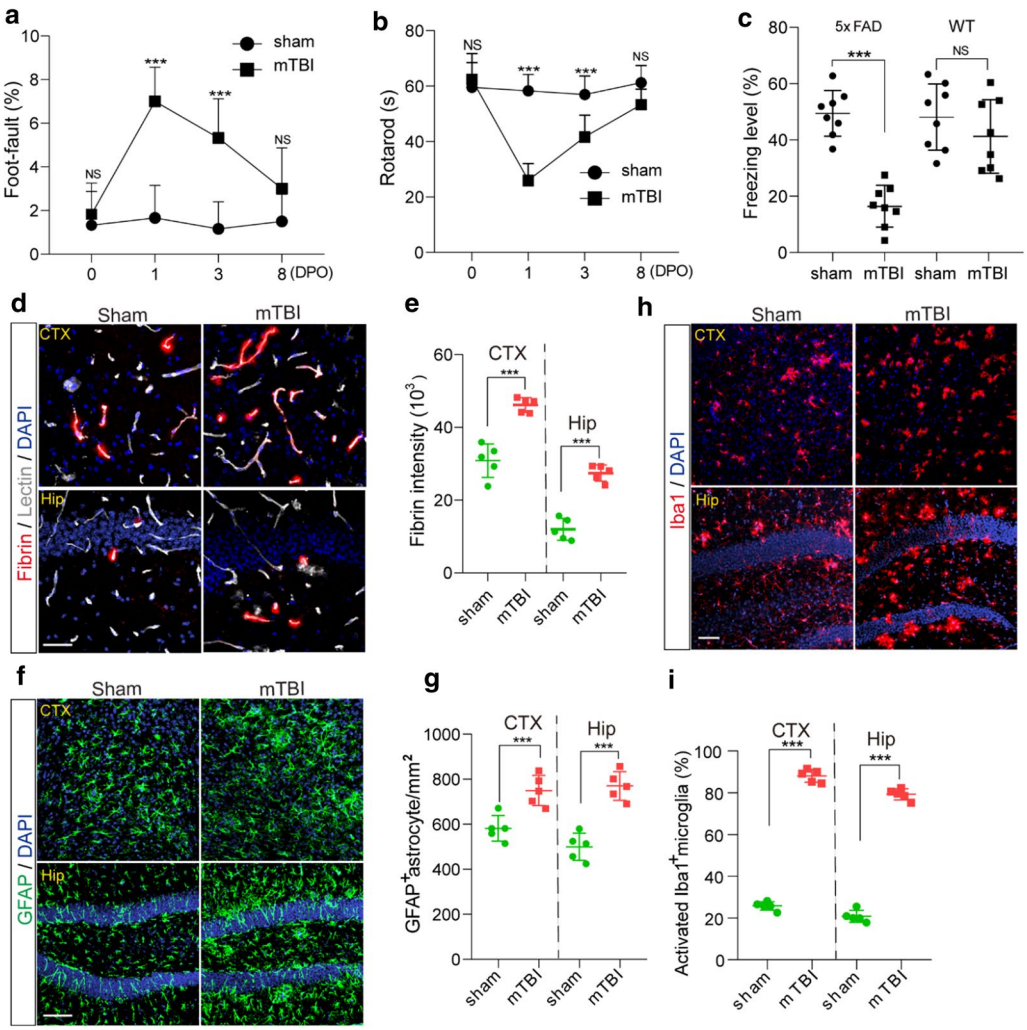

Fig. 5 Accelerated cognitive impairment and pathologies in 5xFAD mice after mTBI. **a**–**b** Foot- fault (**A**) and Rotarod (**b**) tests were performed in 3 months old 5xFAD mice on 0, 1, 3 and 8 days after mTBI or sham-operation. $n = 8$ mice per time point per group. **c** Contextual fear conditioning test was performed in 3 months old 5xFAD mice 8 days after mTBI or sham-operation as in (**a**–**b**)**,** or in non-transgenic littermates (WT) 8 days after mTBI or sham-operation. $n = 8$ mice per group. **d**–**e** Representative images (**d**) and quantification (**e**) showing extravascular fibrin deposits in brain parenchyma 8 days after mTBI, in both cortex (CTX) and hippocampus (Hip). Lectin (gray), fibrin (red). $n = 5$ mice; Scale bar = 50 μm. **f**–**g** Representative images (**f**) and quantification (**g**) showing GFAP-positive astrocytes in brain parenchyma 8 days after mTBI. GFAP (green). $n = 5$ mice per group; Scale bar = 50 μm. **h** Representative images of fluorescence immunostaining for microglial marker Iba1 (red) and DAPI (blue) in brain parenchyma 8 days after mTBI. Scale bar = 50 μm. **i** Quantification for the percentage of activated Iba1 positive cells in both cortex and hippocampus ($n = 5$ mice per group). In **a**–**b**, Mean ± SD; ***, $P < 0.001$, NS, non-significant ($P > 0.05$), one-way ANOVA followed by Bonferroni's post-hoc tests. In **c**, **e**, **g**, **i**, Mean ± SD; ***, $P < 0.001$, NS, non-significant ($P > 0.05$) by Student's *t*-test

mTBI exacerbated BBB breakdown, amyloid pathologies and cognitive impairment in 5xFAD mice

Prominent amyloid pathologies are found in at least 30% of TBI patients [42]. Next, we conducted mTBI in the 5xFAD mouse model of AD at 3 months of age, where amyloid pathology is evident but cognitive function remains relatively normal [22]. Longitudinal behavioral tests in the acute/subacute phase of mTBI indicated that the 5xFAD mice had a transient impairment in motor coordination at 1 DPO but soon recovered nearly back to normal in 8 days, as shown by rotarod and foot fault tests (Fig. 5a, b). However, these 5xFAD mice suffered substantially from cognitive impairment at 8 DPO, as shown by a reduction in freezing time based on contextual fear conditioning test (Fig. 5c), when compared with sham-operated 5xFAD mice or wild type littermates (WT).

More importantly, mTBI exacerbated the BBB dysfunction in 5xFAD mice [32], as shown by > 53.3%

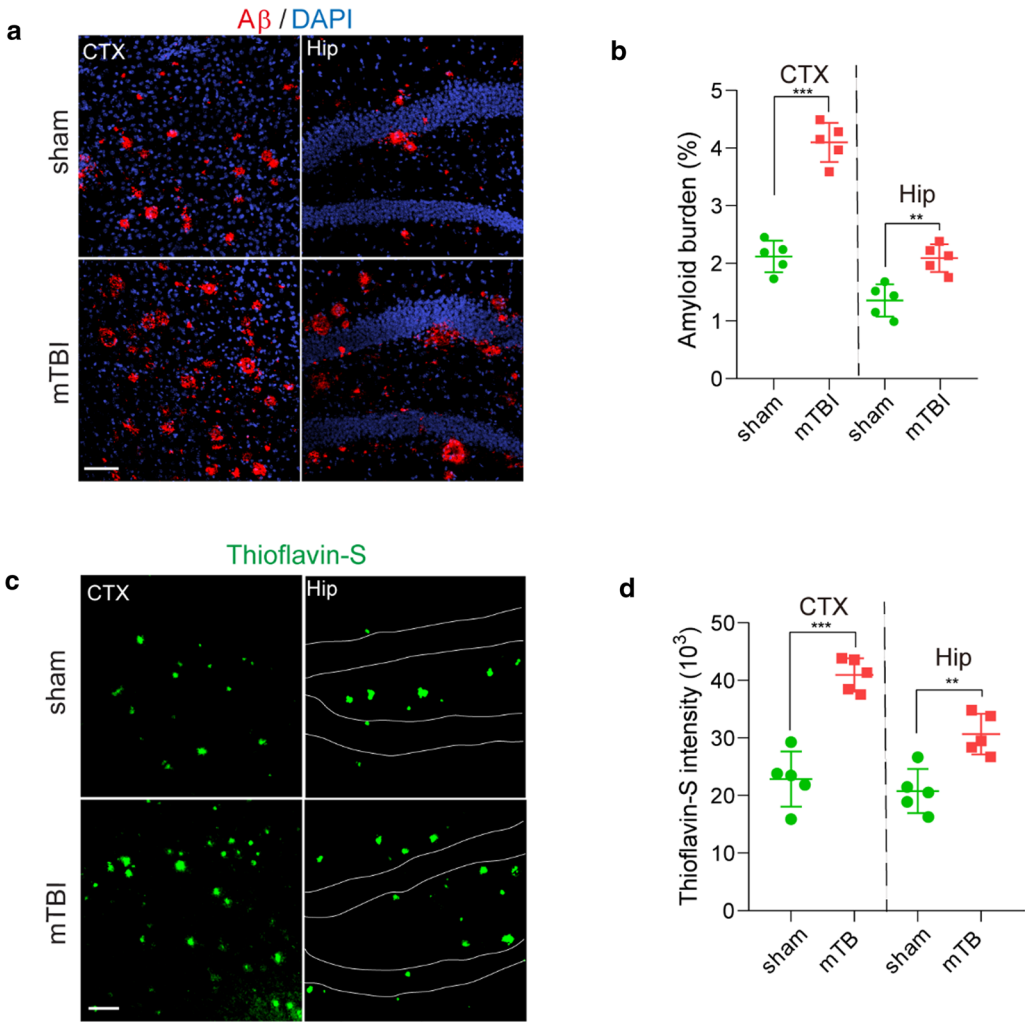

Fig. 6 Accelerated amyloid pathology in 5xFAD mice after mTBI. **a**–**b** Representative images (**A**) showing immunostaining of brain amyloid deposits (red), DAPI (blue) and quantification (**b**) for the amyloid burden (based on the percentage of cortical area occupied with Aβ immunostaining) in cortex (CTX) and Hippocampus (Hip) area 8 days post operation. $n = 5$ mice per group, scale bar = 100 μm. **s**–**d** Representative images (**c**) showing Thioflavin-S labelled amyloid plaques (green) and quantification for the intensity of Thioflavin-S (**d**) in cortex (CTX) and Hippocampus (Hip) area 8 days post operation. $n = 5$ mice per group, scale bar = 100 μm. In **b** and **d**, data are presented as Mean ± SD; ***, $P < 0.001$; **, $P < 0.01$; by Student's *t*-test

extravascular fibrin deposits in both mTBI affected cortex and hippocampus when compared with sham-operated mice at 8 DPO (Fig. 5d, e). Additionally, mTBI resulted in gliosis changes in cortex and hippocampus, as indicated by significant increases in both astrocytes (Fig. 5f, g) and activated microglia cells at 8 DPO (Fig. 5h, i). Using histological analysis, we found that the amyloid burden in mTBI mice was nearly doubled in both cortex and hippocampus 8 days after mTBI (Fig. 6a, b), when compared with sham-operated 5xFAD mice. This is consistent with increased Thioflavin-S positive amyloid plaques (Fig. 6c, d), and demonstrates that mTBI exacerbated the amyloid pathologies in 5xFAD mice.

Discussion

Microvascular injury and BBB impairment are commonly found across neurodegenerative conditions, including but not limited to TBI, stroke, AD, amyotrophic lateral sclerosis (ALS), multiple sclerosis (MS) and even aging [20], although the etiology in each condition could be rather distinct [21]. Vascular impairments induced by mTBI have been well documented both clinically in patients and preclinically in animal models, but the underlying mechanism has not been clearly understood. In the present study, we evaluated the microvascular injury, BBB disruption and pathologic changes in the acute/subacute stage in a rodent mTBI model, and compared with

the sTBI model. We noted enlarged perivascular spaces surrounding blood vessels ipsilateral to mTBI as well as a significant increase in perivascular extravasation of plasma proteins, pericyte loss and reduced CBF. These data are indicative of a compromised cerebral microvasculature, as well as a leaky and malfunctioning BBB. We then used the 5xFAD mouse model of AD to further clarify the link between mTBI and AD, and found mTBI exacerbated BBB leakage, amyloid pathology and cognitive deficits post injury. In conclusion, our study demonstrated that mTBI induces BBB dysfunction, damages the perivascular basement membrane, and aggravates neuropathologies and cognitive deficiencies associated with AD.

It is reported that mTBI induces relatively sustained shear stress located within a discrete region near the impact contact zone [43], which contributes to acute and/or subacute brain pathologies, including microvascular injury and BBB disruption [4]. Subsequently, mTBI can elicit a complex sequence of cellular cascades, and lead to genomic responses and transcriptional changes in vascular cells [38], including vascular endothelial growth factor A (VEGFA), and compensatory changes in the extracellular matrix proteins and expansion of the basal lamina [37], which not only alter the basement membrane structure and perivascular space but also affect brain infiltration of peripheral leukocytes. Recent evidence from RNA sequencing of brain endothelial cells in different animal models has demonstrated that similar vascular gene expression profiles exist among multiple neurodegenerative diseases including TBI [38], suggesting perhaps that the molecular signature of vascular impairment might be common. Nevertheless, future studies exploring vascular associated transcriptomic changes at single-cell level in both mouse models and human patients are necessary for defining the exact microvascular molecular signature in mTBI, and beyond.

There has been growing attention to mTBI and the development of dementia later in life [44]. Potential underlying mechanisms between TBI and later development of AD include diffused axonal damage, persistent inflammation and vascular dysfunctions [5, 45]. While aberrant Tau pathology induced by TBI is considered a high-risk factor for chronic traumatic encephalopathy (CTE), the production and accumulation of brain Aβ species are still considered as the main pathophysiological link between TBI and AD. Our study is the first to establish an mTBI model in 5xFAD mice and described the cognitive impairment and amyloid pathologies in the subacute phase following mTBI. We overserved that amyloid pathology and hippocampal dependent memory impairment was exacerbated within 8 days after mTBI in 3–4 months old 5xFAD mice when compared to the sham-operated group, which was largely consistent with previous studies using different transgenic models [46]. Aβ peptides are produced by neurons and other cell types, and they are subsequently eliminated via several clearance pathways including receptor-mediated transport across the BBB to the peripheral circulation, enzyme-mediated Aβ proteolytic degradation and removal by glial cells, and the perivascular drainage pathway for passive diffusion that connects to the meningeal lymphatic system [21]. Therefore, our data suggest that mTBI may alter the balance between Aβ production and clearance in the brain.

The cerebrovascular system plays a key role in removing metabolic waste products and toxic proteins such as Aβ from the brain [20]. As Aβ homeostasis sustained by vascular clearance pathways are integrated functions of normal cerebrovascular structure and an intact BBB [21], the loss of vascular integrity could play a key role in AD pathogenesis, as well as the mediation of tissue damage after TBI. While most current studies point to vascular injury after TBI, it remains unclear whether vascular impairment and BBB disruption induced by TBI affects the balance between amyloid production and clearance in the brain, and lead to cognitive impairment and dementia. Our study in 5xFAD mice demonstrated that mTBI exacerbates microvascular injury and BBB dysfunction in addition to existing vascular dysfunctions. Decreased BBB expression of amyloid receptors including Lipoprotein-related receptor protein 1 (LRP1) and P-glycoprotein [42] have been previously reported in TBI rodent models, suggesting increased brain amyloid production and decreased transvascular clearance occur simultaneously after TBI. Furthermore, repetitive injury is a very important aspect of TBI, and the second impact may elicit much stronger deficits in BBB, CBF and clearance. Thus, future studies are required to systematically determine the imbalance between Aβ production, perivascular drainage and transvascular clearance for a better understanding of TBI-induced Aβ pathogenesis and increased risk for AD, and whether vascular-directed therapies to restore BBB integrity and clearance functions can reduce the risk of TBI-related neurodegenerative diseases. It will be also interesting to examine the vascular impairment in repetitive settings and long-term effects on neurodegeneration, and compare the differential outcomes between young and aged mice.

Conclusion

In conclusion, our study demonstrated that mTBI can induce BBB dysfunction and pericytes loss, impair the perivascular structure, exacerbate amyloid pathologies and cognitive decline in mice.

Abbreviations
AD: Alzheimer's disease; Aβ: β-Amyloid; ALS: Amyotrophic lateral sclerosis; ANOVA: Analysis of variance; BBB: Blood–brain barrier; CBF: Cerebral blood flow; CD13: Cluster of differentiation 13; CNS: Central nervous system; CTE: Chronic traumatic encephalopathy; DAPI: 4′,6-Diamidino-2-phenylindole; DG: Dentate gyrus; DPO: Days post operation; ER: Endoplasmic reticulum; GFAP: Glial fibrillary acidic protein; ISF: Interstitial fluid; LSCI: Laser speckle contrast imaging; LRP1: Lipoprotein-related receptor protein 1; mTBI: Mild traumatic brain injury; MS: Multiple sclerosis; PBS: Phosphate-buffered saline; PFA: Paraformaldehyde; ROIs: Regions of interest; sTBI: Severe traumatic brain injury; TBI: Traumatic brain injury; TUNEL: Terminal deoxynucleotidyl transferase dUTP nick end labeling; VEGF: Vascular endothelial growth factor; WT: Wild type.

Supplementary Information

The online version contains supplementary material available at https://doi.org/10.1186/s40478-021-01178-7.

Additional file 1: Supplementary figures. **Supplementary Fig. 1** Traumatic brain injury models with controlled cortical impact in mice. (A) The timeline for the establishment of the TBI mouse model and the other experimental procedures. (B) Brain precision impactor device (RWD Life Science) to establish mTBI mouse model. (C-D) The experimental parameters used in the establishment of TBI mouse models. **Supplementary Fig. 2** Neuropathological changes 3 days after sTBI or mTBI in mouse model. (A) Cerebral edema measured by brain water content. The injury significantly induced the development of cerebral edema at 24 hours post-injury in sTBI model compared to mTBI model. n = 8 mice per group, Data are presented as Mean ± SD; ***, $P < 0.001$; NS, non-significant ($P > 0.05$), one-way ANOVA followed by Bonferroni's post-hoc tests. (B) Representative confocal images showing NeuN (green) staining and TUNEL assay (red) for apoptotic neuronal death in the impacted ipsilateral area after sTBI and mTBI, or sham-operation. Scale bar, 50 μm. (C) Quantification of the percentage of TUNEL-positive neuronal death in sTBI (n = 6 mice) or mTBI (n = 6 mice). Data are presented as Mean ± SD; *** $P < 0.001$ by Student's t-test. Dash line indicates an average value from sham-operated group (n = 3 mice). (D-E) Representative immunoblots (D) and quantification (E) of Synapsin I from the cortex in the injury ipsilateral side of sham-operated, mTBI and sTBI mice. β-Actin: loading control. Data are presented as Mean ± SD; n = 3 mice per group respectively; ***, $P < 0.001$; **, $P < 0.01$; one-way ANOVA followed by Bonferroni's post-hoc tests. **Supplementary Fig. 3** Neuroinflammatory changes 3 days after sTBI or mTBI in mouse model. (A) Representative images of fluorescence immunostaining for Iba1 (gray) and DAPI (blue), boxed regions show an activated and phagocytotic microglia (a1, a3) in the impacted ipsilateral side, and ramified microglia at resting state (a2, a4) in the contralateral side. Scale bar in (A) 50 μm, in (a1-a6) 10 μm. (B) Quantification for the percentage of activated Iba1 positive cells (n = 6 mice per group) in the impact side (ipsi) and contralateral side (contra) in sTBI and mTBI mice (see method). Dash line indicates the average value from the sham-operated group (n = 5 mice). (C) Representative images of fluorescence immunostaining for GFAP (green) and DAPI (blue), boxed regions (c1-c4) show astrocytes in the impact side and the contralateral side. Scale bar in (C) 50 μm, in (c1-c6) 10 μm. (D) Quantification for the GFAP positive cells per mm2 (n = 6 mice per group) in the impact side (ipsi) and contralateral side (contra) in sTBI and mTBI mice. Dash line indicates the average value from sham-operated group (n = 5 mice). Data are presented as Mean ± SD; ***, $P < 0.001$; **, $P < 0.01$; *, $P < 0.05$; NS, non-significant ($P > 0.05$) by by Student's *t*-test. **Supplementary Fig. 4** Vascular impairment in the subacute phase of mTBI in mice. (A-B) Representative images (A) and quantification (B) showing extravascular fibrin deposits in brain parenchyma 3 days after mTBI. Lectin (gray), fibrin (red). n = 7 mice; Scale bar = 20 μm. (C-D) Representative images (C) and quantification (D) showing extravasation of intravenously administrated Alexa-555 cadaverine (red) in brain parenchyma 3 days after mTBI. Lectin (green), n = 7 mice, scale bar = 50 μm. In B, D, data are presented as Mean ± SD; ***, $P < 0.001$ by Student's t-test. Dash lines indicate average value from sham-operated group (n = 3 mice). (E-F) Cerebral blood flow reduction 3 days after mTBI. Representative laser speckle contrast imaging (LSCI) images (E) and quantification of boxed regions (F) showing blood flow changes in the cortical regions 3 days after mTBI. Scale bar = 50 μm. **Supplementary Fig. 5** The time course of microglial activation after mTBI in mice. (A) Representative confocal microscope images showing Iba1-positive microglia cells (red) in cortex (CTX), Cornu Ammonis 1 (CA1) and dentate gyrus (DG) area 1-day, 3- and 8- days post operation (DPO). Scale bar = 100 μm. (B-D) Quantification for the Iba1-positive microglia cells per mm^2 (n = 5 mice per time point) in CTX, CA1 and DG area 1 day, 3- and 8-days post operation (DPO). Data are presented as Mean ± SD; ***, $P < 0.001$; **, $P < 0.01$; one-way ANOVA followed by Bonferroni's post-hoc tests.

Acknowledgments
The authors would like to thank the RWD Life Science for assisting the Laser Speckle Contrast Imaging, Dr. Berislav Zlokovic and Dr. Yaoming Wang for guidance and technical support, and Dr. Zhonghua Dai for careful reading of the manuscript and critical comments.

Authors' contributions
YW, HW and ZZ designed and performed experiments and analyzed data and wrote the manuscript. JZ, SD, XX, XG, TG, SF and YY performed experiments. BP, XG, XL, JFC, NSM, QM, and FGP contributed to writing the manuscript. All authors read and approved the final manuscript.

Funding
This work was partly supported by the National Institutes of Health (NIH) grant 1R01NS112404 to Q.M., NIH grant RF1NS122060, the Alzheimer's Association (NIRG-15–363387) and BrightFocus Foundation (A2019218S) to Z.Z.

Availability of data and materials
The data that support the findings of this study are available from the corresponding author upon request.

Declarations

Ethics approval and consent to participate
The animal experiments were approved by the Institutional Animal Care and Use Committee at the University of Southern California per NIH guidelines.

Competing interests
The authors declare that they have no competing interests.

Author details
[1]Center for Neurodegeneration and Regeneration, Zilkha Neurogenetic Institute, Room: 241, 1501 San Pablo Street, Los Angeles, CA 90033, USA. [2]Department of Physiology and Biophysics, Keck School of Medicine, University of Southern California, Los Angeles, CA 90033, USA. [3]Department of Neurosurgery, Second Affiliated Hospital, School of Medicine, Zhejiang University, Hangzhou 310009, Zhejiang, China. [4]Neuroscience Graduate Program, Keck School of Medicine, University of Southern California, Los Angeles, CA 90033, USA. [5]Center for Craniofacial Molecular Biology, Herman Ostrow School of Dentistry, University of Southern California, Los Angeles, CA 90033, USA. [6]Lawrence D. Longo, MD Center for Perinatal Biology, Division of Pharmacology, Department of Basic Sciences, Loma Linda University School of Medicine, Loma Linda, CA 92350, USA. [7]Brain Injury Research Center, Department of Neurosurgery, University of California, Los Angeles, Los Angeles, CA 90095, USA.

Received: 3 March 2021 Accepted: 10 April 2021
Published online: 23 April 2021

References

1. Jack CR, Bennett DA, Blennow K, Carrillo MC, Dunn B, Haeberlein SB et al (2018) NIA-AA research framework: toward a biological definition of Alzheimer's disease. Alzheimers Dement J Alzheimers Assoc 14:535–562
2. Goate A, Hardy J (2012) Twenty years of Alzheimer's disease-causing mutations: APP mutations after 20 years. J Neurochem 120:3–8
3. Association Alzheimer's (2019) Alzheimer's disease facts and figures. Alzheimers Dement 15:321–387. https://doi.org/10.1016/j.jalz.2019.01.010

4. Sandsmark DK, Bashir A, Wellington CL, Diaz-Arrastia R (2019) Cerebral microvascular injury: a potentially treatable endophenotype of traumatic brain injury-induced neurodegeneration. Neuron 103:367–379
5. Blennow K, Hardy J, Zetterberg H (2012) The neuropathology and neurobiology of traumatic brain injury. Neuron 76:886–899
6. Wu Y, Wu H, Guo X, Pluimer B, Zhao Z (2020) Blood–brain barrier dysfunction in mild traumatic brain injury: evidence from preclinical murine models. Front Physiol 11:1030
7. Kenney K, Diaz-Arrastia R (2018) Risk of dementia outcomes associated with traumatic brain injury during military service. JAMA Neurol 75:1043–1044. https://doi.org/10.1001/jamaneurol.2018.0347
8. Scott G, Ramlackhansingh AF, Edison P, Hellyer P, Cole J, Veronese M et al (2016) Amyloid pathology and axonal injury after brain trauma. Neurology 86:821–828
9. Yu F, Zhang Y, Chuang D-M (2012) Lithium reduces BACE1 overexpression, β amyloid accumulation, and spatial learning deficits in mice with traumatic brain injury. J Neurotrauma 29:2342–2351
10. Furuya Y, Hlatky R, Valadka AB, Diaz P, Robertson CS (2003) Comparison of cerebral blood flow in computed tomographic hypodense areas of the brain in head-injured patients. Neurosurgery. 52:340–345 (**discussion 345–346**)
11. Menon DK (2006) Brain ischaemia after traumatic brain injury: lessons from 15O2 positron emission tomography. Curr Opin Crit Care 12:85–89
12. Wilson L, Stewart W, Dams-O'Connor K, Diaz-Arrastia R, Horton L, Menon DK et al (2017) The chronic and evolving neurological consequences of traumatic brain injury. Lancet Neurol 16:813–825
13. Corrigan JD, Hammond FM (2013) Traumatic brain injury as a chronic health condition. Arch Phys Med Rehabil 94:1199–1201
14. Villalba N, Sackheim AM, Nunez IA, Hill-Eubanks DC, Nelson MT, Wellman GC et al (2017) Traumatic brain injury causes endothelial dysfunction in the systemic microcirculation through arginase-1–dependent uncoupling of endothelial nitric oxide synthase. J Neurotrauma 34:192–203
15. Bhowmick S, D'Mello V, Caruso D, Wallerstein A, Abdul-Muneer PM (2019) Impairment of pericyte-endothelium crosstalk leads to blood-brain barrier dysfunction following traumatic brain injury. Exp Neurol 317:260–270
16. Foley LM, O'Meara AMI, Wisniewski SR, Hitchens TK, Melick JA, Ho C et al (2013) MRI assessment of cerebral blood flow after experimental traumatic brain injury combined with hemorrhagic shock in mice. J Cereb Blood Flow Metab 33:129–136
17. Alluri H, Wilson RL, Anasooya Shaji C, Wiggins-Dohlvik K, Patel S, Liu Y et al (2016) Melatonin preserves blood-brain barrier integrity and permeability via matrix metalloproteinase-9 inhibition. PLoS ONE 11:e0154427
18. Shi H, Wang H-L, Pu H-J, Shi Y-J, Zhang J, Zhang W-T et al (2015) Ethyl pyruvate protects against blood-brain barrier damage and improves long-term neurological outcomes in a rat model of traumatic brain injury. CNS Neurosci Ther 21:374–384
19. Schwarzmaier SM, Zimmermann R, McGarry NB, Trabold R, Kim S-W, Plesnila N (2013) In vivo temporal and spatial profile of leukocyte adhesion and migration after experimental traumatic brain injury in mice. J Neuroinflammation 10:32
20. Zhao Z, Nelson AR, Betsholtz C, Zlokovic BV (2015) Establishment and dysfunction of the blood-brain barrier. Cell 163:1064–1078
21. Sweeney MD, Zhao Z, Montagne A, Nelson AR, Zlokovic BV (2019) Blood-brain barrier: from physiology to disease and back. Physiol Rev 99:21–78
22. Dinkins MB, Dasgupta S, Wang G, Zhu G, He Q, Kong JN et al (2015) The 5XFAD mouse model of Alzheimer's disease exhibits an age-dependent increase in anti-ceramide IgG and exogenous administration of ceramide further increases anti-ceramide titers and amyloid plaque burden. J Alzheimers Dis JAD 46:55–61
23. Ojo J-O, Mouzon B, Greenberg MB, Bachmeier C, Mullan M, Crawford F (2013) Repetitive mild traumatic brain injury augments tau pathology and glial activation in aged hTau mice. J Neuropathol Exp Neurol 72:137–151
24. Romine J, Gao X, Chen J (2014) Controlled cortical impact model for traumatic brain injury. J Vis Exp JoVE 90:e51781
25. Zhang L, Schallert T, Zhang ZG, Jiang Q, Arniego P, Li Q et al (2002) A test for detecting long-term sensorimotor dysfunction in the mouse after focal cerebral ischemia. J Neurosci Methods 117:207–214
26. Lazic D, Sagare AP, Nikolakopoulou AM, Griffin JH, Vassar R, Zlokovic BV (2019) 3K3A-activated protein C blocks amyloidogenic BACE1 pathway and improves functional outcome in mice. J Exp Med 216:279–293
27. Wang Y, Zhao Z, Chow N, Rajput PS, Griffin JH, Lyden PD et al (2013) Activated protein C analog protects from ischemic stroke and extends the therapeutic window of tissue-type plasminogen activator in aged female mice and hypertensive rats. Stroke J Cereb Circ 44:3529–3536
28. Armulik A, Genové G, Mäe M, Nisancioglu MH, Wallgard E, Niaudet C et al (2010) Pericytes regulate the blood–brain barrier. Nature 468:557–561
29. Dash PK, Zhao J, Kobori N, Redell JB, Hylin MJ, Hood KN et al (2016) Activation of Alpha 7 cholinergic nicotinic receptors reduce blood-brain barrier permeability following experimental traumatic brain injury. J Neurosci Off J Soc Neurosci 36:2809–2818
30. Winship IR (2014) Laser speckle contrast imaging to measure changes in cerebral blood flow. Methods Mol Biol Clifton NJ 1135:223–235
31. Lan X, Han X, Li Q, Yang Q-W, Wang J (2017) Modulators of microglial activation and polarization after intracerebral haemorrhage. Nat Rev Neurol 13:420–433
32. Nikolakopoulou AM, Zhao Z, Montagne A, Zlokovic BV (2017) Regional early and progressive loss of brain pericytes but not vascular smooth muscle cells in adult mice with disrupted platelet-derived growth factor receptor-β signaling. PLoS ONE 12:e0176225
33. Miao W, Zhao Y, Huang Y, Chen D, Luo C, Su W et al (2020) IL-13 ameliorates neuroinflammation and promotes functional recovery after traumatic brain injury. J Immunol Baltim Md 2020(204):1486–1498
34. Libbey JE, Lane TE, Fujinami RS (2014) Axonal pathology and demyelination in viral models of multiple sclerosis. Discov Med 18:79–89
35. Shlosberg D, Benifla M, Kaufer D, Friedman A (2010) Blood–brain barrier breakdown as a therapeutic target in traumatic brain injury. Nat Rev Neurol 6:393–403
36. Obenaus A, Ng M, Orantes AM, Kinney-Lang E, Rashid F, Hamer M et al (2017) Traumatic brain injury results in acute rarefication of the vascular network. Sci Rep 7:1–14
37. Meng Q, Zhuang Y, Ying Z, Agrawal R, Yang X, Gomez-Pinilla F (2017) Traumatic brain injury induces genome-wide transcriptomic, methylomic, and network perturbations in brain and blood predicting neurological disorders. EBioMedicine 16:184–194
38. Munji RN, Soung AL, Weiner GA, Sohet F, Semple BD, Trivedi A et al (2019) Profiling the mouse brain endothelial transcriptome in health and disease models reveals a core blood-brain barrier dysfunction module. Nat Neurosci 22:1892–1902
39. Hannocks M-J, Pizzo ME, Huppert J, Deshpande T, Abbott NJ, Thorne RG et al (2018) Molecular characterization of perivascular drainage pathways in the murine brain. J Cereb Blood Flow Metab 38:669–686
40. Thyboll J, Kortesmaa J, Cao R, Soininen R, Wang L, Iivanainen A et al (2002) Deletion of the Laminin 4 chain leads to impaired microvessel maturation. Mol Cell Biol 22:1194–1202
41. Yao Y, Chen Z-L, Norris EH, Strickland S (2014) Astrocytic laminin regulates pericyte differentiation and maintains blood brain barrier integrity. Nat Commun 5:1–12. https://doi.org/10.1038/ncomms4413
42. Pop V, Sorensen DW, Kamper JE, Ajao DO, Murphy MP, Head E et al (2013) Early brain injury alters the blood–brain barrier phenotype in parallel with β-amyloid and cognitive changes in adulthood. J Cereb Blood Flow Metab 33:205–214
43. Tagge CA, Fisher AM, Minaeva OV, Gaudreau-Balderrama A, Moncaster JA, Zhang X-L et al (2018) Concussion, microvascular injury, and early tauopathy in young athletes after impact head injury and an impact concussion mouse model. Brain J Neurol 141:422–458
44. Fleminger S, Oliver DL, Lovestone S, Rabe-Hesketh S, Giora A (2003) Head injury as a risk factor for Alzheimer's disease: the evidence 10 years on; a partial replication. J Neurol Neurosurg Psychiatry 74:857–862
45. Ramos-Cejudo J, Wisniewski T, Marmar C, Zetterberg H, Blennow K, de Leon MJ et al (2018) Traumatic brain injury and Alzheimer's disease: the cerebrovascular link. EBioMedicine 28:21–30
46. Edwards G, Moreno-Gonzalez I, Soto C (2017) Amyloid-beta and tau pathology following repetitive mild traumatic brain injury. Biochem Biophys Res Commun 483:1137–1142

Publisher's Note